Supporting Information

Atomically Dispersed Ru on Defective CdS for Photocatalytic Solar Fuel Production Coupled with Hydrazine Degradation

*Zikang Zeng,[a] Siyu Kang,[a] Xiaohe Jiang,[a] Hai Qiu,[b] Yu-Chia Chang,[c] Yu-Ting Chueh,[c] Lan Yuan,[*b] Yujun Liang,[a] Jianguo Chang,[*d] Gui Yang,[e] Sung-Fu Hung[*c] and Chuang Han[*a]*

[a] *Faculty of Materials Science and Chemistry, China University of Geosciences, Wuhan 430074, China*

[b] *Key Laboratory of Hubei Province for Coal Conversion and New Carbon Materials, Wuhan University of Science and Technology, Wuhan 430081, China*

[c] *Department of Applied Chemistry, National Yang Ming Chiao Tung University, Hsinchu 300, Taiwan*

[d] *Faculty of Anhui Key Laboratory of Green Carbon Chemistry, Fuyang Normal University, Fuyang 236037, China*

[e] *Faculty of Environmental Science and Engineering, Kunming University of Science and Technology, Kunming 650500, China*

*Corresponding Author: yuanlan@wust.edu.cn (*Lan Yuan*); jgchang@fynu.edu.cn (*Jianguo Chang*); sungfuhung@nycu.edu.tw (*Sung-Fu Hung*); hanc@cug.edu.cn (*Chuang Han*)

Contents list:

Experimental Section

Characterization

The powder X-ray diffraction (XRD) patterns of the catalysts were obtained using an X-ray diffraction instrument (D8-FOCUS, Bruker, Germany) with Cu-Kα radiation (λ = 1.5418 Å), scanning in the range of 5°-80° at a scanning rate of 5 °/min. The morphology and microstructure of the prepared samples were analyzed using field emission scanning electron microscopy (SEM, Japan SU8010) and transmission electron microscopy (TEM, America G2 T20). High-angle annular dark-field scanning transmission electron microscopy (HAADF-STEM) was conducted using an image- and probe-corrected transmission electron microscope operating at 200 kV (FEI Themis 60–300). X-ray absorption spectroscopy, encompassing X-ray absorption near edge spectra (XANES) and extended X-ray absorption fine structure (EXAFS) for Ru K-edge, was conducted in a fluorescence mode at room temperature at BL-12B2 in SPring-8, NSRRC. Least-squares curve fitting analysis of the EXAFS data was performed using the Artemis program. X-ray photoelectron spectroscopy (XPS) data were acquired using an Al Kα excitation source from Thermo Fisher Scientific. UV-vis diffuse reflectance spectra (DRS) were measured in the range of 200-800 nm on a scanning UV-vis spectrophotometer (UV-2550PC, Shimadzu), using $BaSO_4$ as the reflectance standard. Photoluminescence (PL) spectra were obtained using a fluorescence spectrometer (Fluoromax-4P, Horiba Jobin Yvon, New Jersey, USA) equipped with a 150 W Xe lamp as the excitation source, with an excitation wavelength of 375 nm. Photoluminescence decay curves were acquired using a Fluorescence Spectrometer (FLS 980, Edinburgh Instruments, Livingston, UK), with a 405 nm-EPLED as the selected light source. Electron Paramagnetic Resonance (EPR) analysis was performed on a Bruker EMX PLUS (Germany) instrument to characterize the content of surface vacancies (V_S) in the materials. The mass fraction of Ru was determined via ICP-MS using an Agilent 7900 instrument; the materials were dissolved in aqua regia and tested after dilution. The in situ Fourier transform infrared (FTIR) spectra were collected on Thermo IS 50 (USA).

Photo-electrochemical measurements:

Photo-electrochemical measurements were collected using a conventional three-electrode electrochemical analyzer (CHI760E, Shanghai). Platinum wire and Ag/AgCl electrodes were used as the counter electrode and reference electrode, respectively. Photocurrent response spectroscopy, linear sweep voltammetry (LSV) curves, open circuit potential, and Mott-Schottky plots were tested using a 0.5 M Na_2SO_4 solution. Electrochemical impedance

spectroscopy (EIS) was tested using a $K_3[Fe(CN)_6]/K_4[Fe(CN)_6]$/KCl (10 mM/10 mM/0.5 M) solution at 0.3 V, –0.8 V and –0.9 V under Xe lamp irradiation. The working electrode was prepared according to the following method: 5 mg of catalyst powder, 200 μL of ethanol, and 20 μL of Nafion solution were mixed and subjected to ultrasonic treatment for 30 min. Finally, the resultant catalyst slurry was coated onto the precleaned FTO glass surface with an active area of 1.00 cm × 1.00 cm and then dried on a 120 ℃ heating stage. For photoelectric current measurements, a 300 W Xe lamp (PLS-SXE 300, Beijing Perfect light Co., Ltd) with a filter (λ > 420 nm) served as the light source, and transient photocurrent responses were measured with a 20 s on/off interval at a bias potential of 0.3 V vs. Ag/AgCl. Transient open-circuit voltage measurements used the same light source as the photocurrent tests. Electrochemical impedance spectroscopy was recorded at a potential of 0.3 V vs. Ag/AgCl, and linear sweep voltammetry (LSV) curves were obtained over a bias range of −1.5 V to 1.5 V vs. Ag/AgCl. The Mott-Schottky plots were recorded at a scanning rate of 5 mV/s and a frequency of 1500, 2000 and 2500 Hz. The reference Ag/AgCl electrode was calibrated against a reversible hydrogen electrode (RHE), and all the potentials herein are reported relative to the RHE, per the following equation.

$$E_{RHE} = E_{Ag/AgCl} + 0.197 + 0.0591 \cdot pH$$

Where E_{RHE} and $E_{\mathrm{Ag/AgCl}}$ are electrode potentials relative to RHE and Ag/AgCl electrode potentials, respectively.

Apparent quantum efficiency (AQE) calculations

The apparent quantum efficiency of CdS-Ru photocatalyst was determined under Xe lamp irradiation at 400, 420, 500, and 600 nm with bandpass filters.

In the photocatalytic reaction, 5 mg of photocatalyst was added to 10 mL of 2 wt.% hydrazine hydrate. The suspension was then purged with Ar (or CO_2) gas for 10 min, and irradiated under monochromatic light of different wavelengths for 1 h. The light power density of the Xe lamp was measured using a radiometer and found to be 14.81, 13.45, 16.31, and 16.80 $mW \cdot cm^{-2}$ at 400, 420, 500, and 600 nm, respectively, with a controlled illumination area of 1 cm^2. The AQE at 400, 420, 500, and 600 nm was calculated as 23.88%, 31.79%, 16.73%, and 2.15% according to the following formula:[1]

$$AQE = \frac{number\ of\ reacted\ electrons}{number\ of\ incident\ photons} \times 100\% = \frac{n\ M\ N_A\ h\ C}{S\ P\ t\ \lambda}$$

n is the electron transfer constant (n = 2 or 6, respectively for H_2 and methanol production);

M represents the mole of produced H_2 or methanol;

$\mathbf{N_A}$ is Avogadro's constant (6.022×10^{23} mol^{-1});

h is Planck's constant (6.626×10^{-34} J·s);

C is the speed of light (3×10^{8} m/s);

S is the irradiation area (cm^2);

P is the power density of incident monochromatic light (W/cm^2);

t is the reaction time (s);

λ is the wavelength of incident monochromatic light (m).

Computational method

We have employed the Vienna Ab initio Simulation Package (VASP) to perform all density functional theory (DFT) calculations within the generalized gradient approximation (GGA) using the Perdew-Burke-Ernzerhof (PBE) functional.[2-5] We have chosen the projected augmented wave (PAW) potentials to describe the ionic cores and take valence electrons into account using a plane wave basis set with a kinetic energy cutoff of 400 eV. Spin-polarization effect was also considered. The DFT-D3 empirical correction method was employed to describe van der Waals interactions.[6] Geometry optimizations were performed with the force convergence smaller than 0.05 eV/Å. Gamma Scheme k-points of 2 × 2 × 1 were applied for all the calculations. All the atoms are relaxed in all the calculations. For Ru-CdS, one Cd in the first layer was replaced by Ru, and one S vacancy was built near Ru according to our experimental observation. The free energy changes (ΔG) of each elementary reaction step during the reaction were calculated using the computational hydrogen electrode (CHE) model. In this model, the chemical potential is equal to the energy of half of the gas-phase H_2 at 0 V vs the reversible hydrogen electrode (RHE). The Gibbs free energy was calculated by the following equation:

$\Delta G = \Delta E + \Delta EZPE - T\Delta S$

Where the value of ΔE, ΔEZPE and ΔS denotes the changes of DFT energy, the zero-point energy and the entropy at 298.15K, respectively.

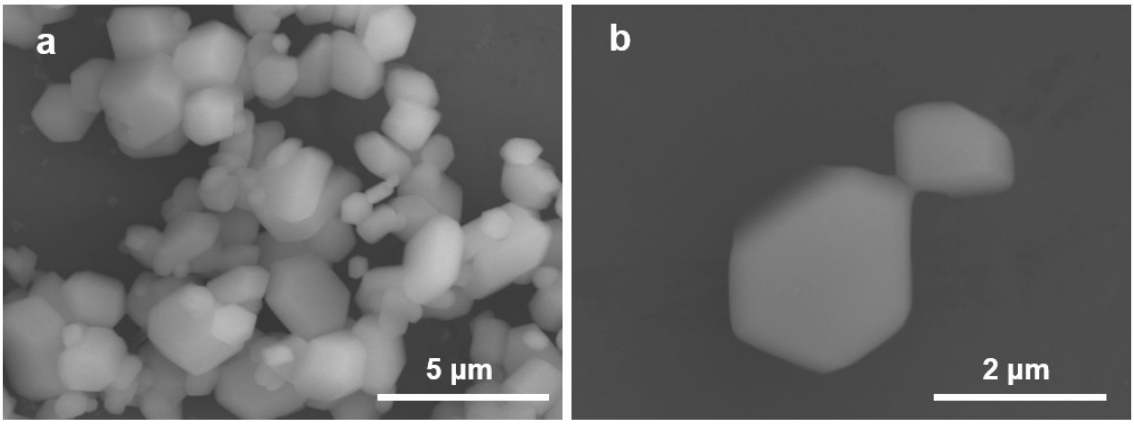

Fig. S1. (a, b) SEM images of ($Cd(S_2CNEt_2)_2$).

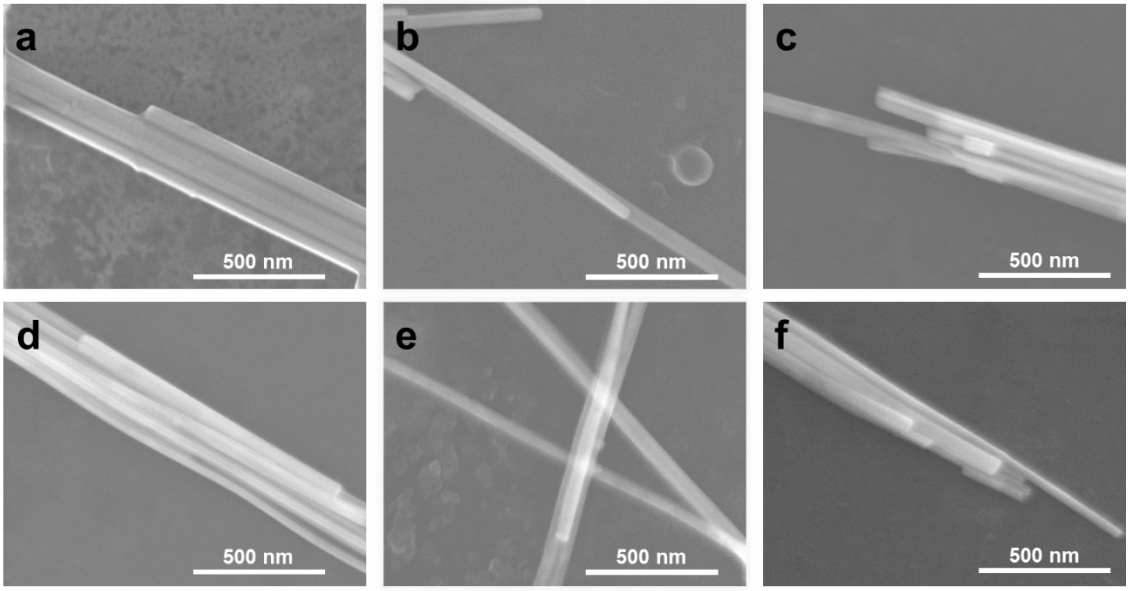

Fig. S2. SEM image of (a) pure CdS, (b) CdS-$Ru_{0.017}$, (c) CdS-$Ru_{0.089}$, (d) CdS-$Ru_{0.18}$, (e) CdS-$Ru_{0.31}$, and (f) CdS-$Ru_{0.57}$.

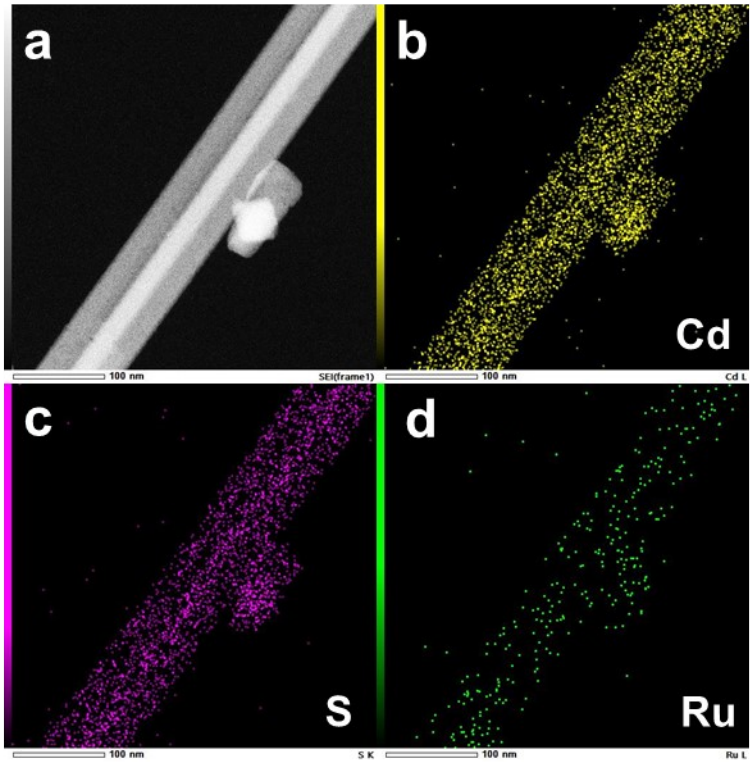

Fig. S3. (a) HAADF-STEM image, (b-d) elemental mapping profiles of CdS-$Ru_{0.089}$ sample.

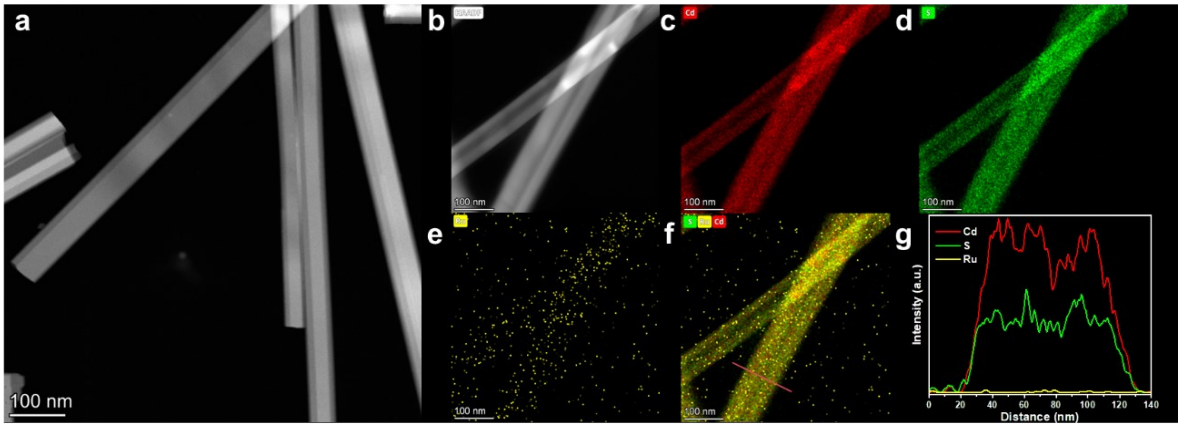

Fig. S4. (a) HAADF-STEM image, (b-f) face-scan elemental mapping profiles and (g) line-scan elemental mapping profiles of CdS-$Ru_{0.57}$ sample.

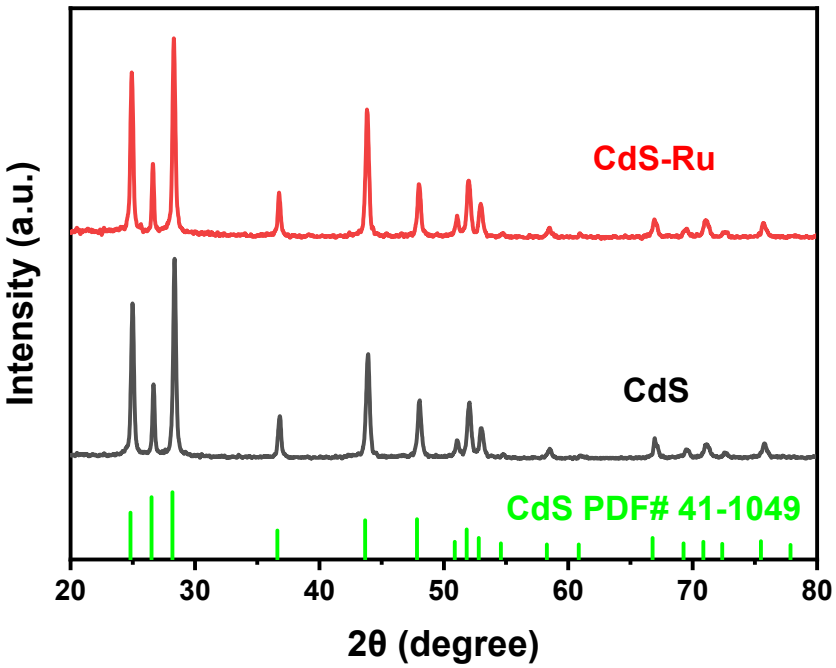

Fig. S5. XRD pattern of CdS and CdS-Ru.

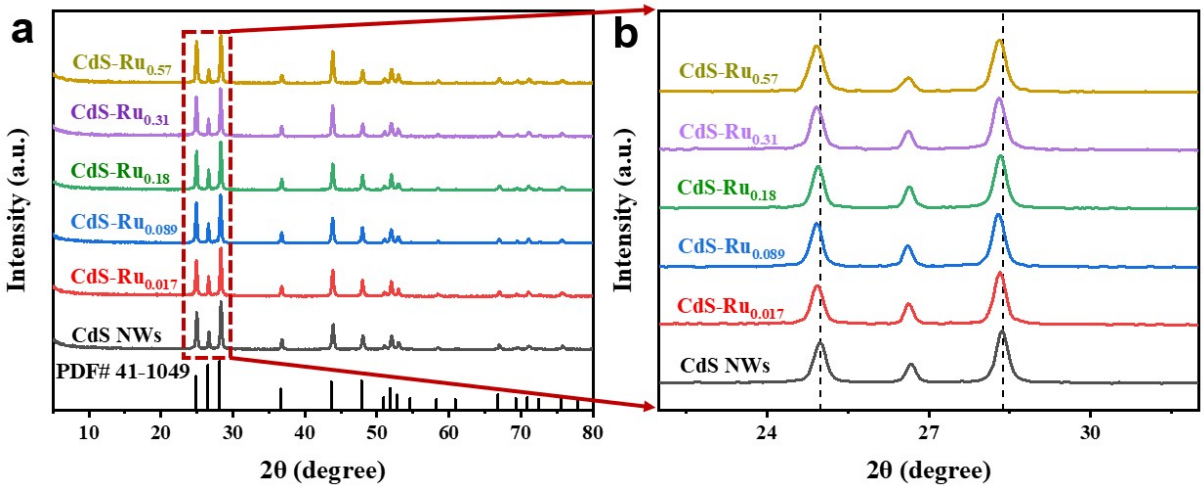

Fig. S6. (a) XRD pattern and (b) detail diagram of CdS-Ru with different Ru loading contents.

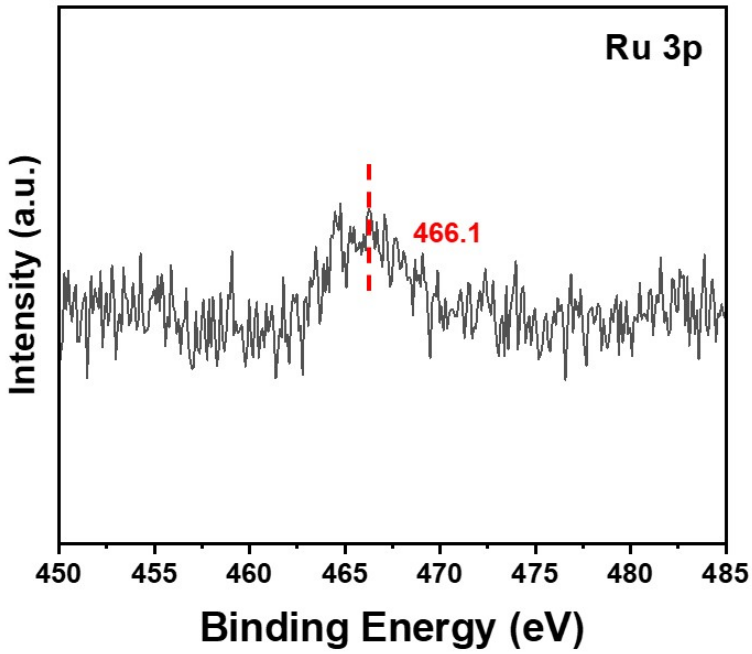

Fig. S7. XPS spectrum of Ru 3p in CdS-Ru.

Note: The adventitious carbon located at 284.8 eV is used to calibrate samples. The weak intensity of the Ru peak is attributed to its low content.

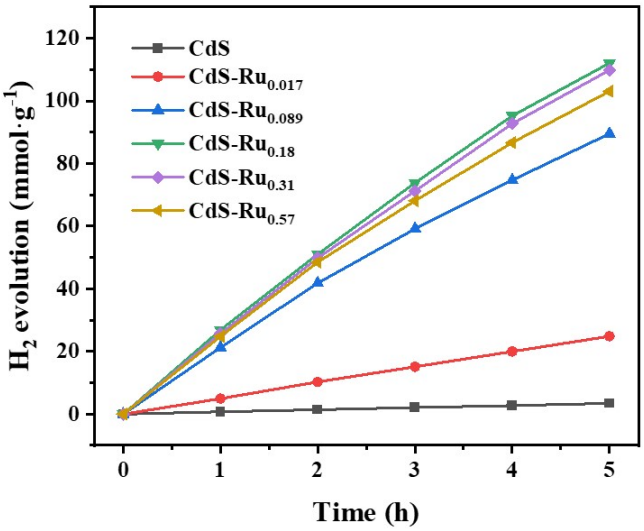

Fig. S8. H_2 production over CdS-Ru with different Ru loading contents. Reaction conditions: 5 mg catalyst, 10 mL 1 wt.% hydrazine hydrate, under LED (60 mW cm^{-2}, $\lambda > 400$ nm) light.

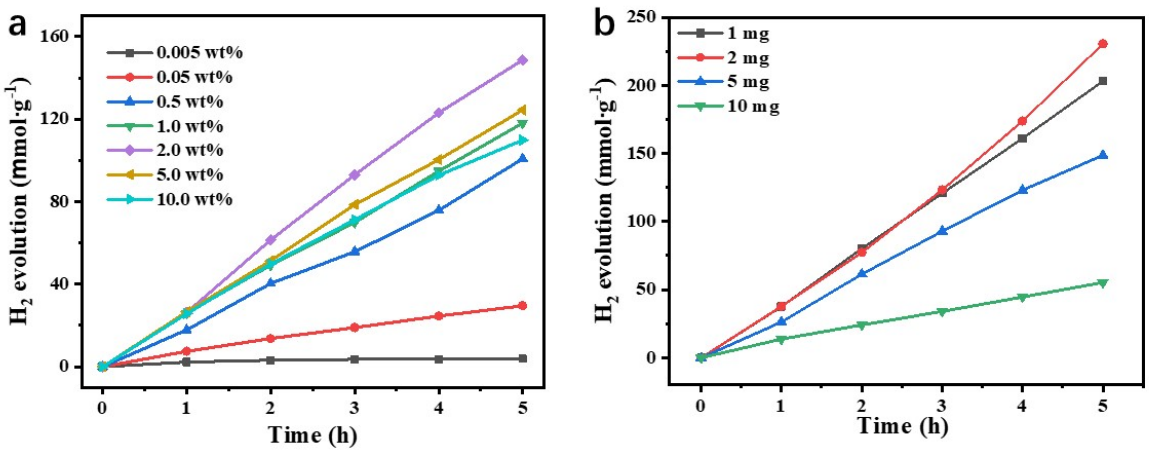

Fig. S9. H_2 production (a) with different concentrations (wt.%) of hydrazine hydrate, (b) with different mass of catalyst under LED light irradiation ($\lambda > 400$ nm, 60 mW cm^{-2}).

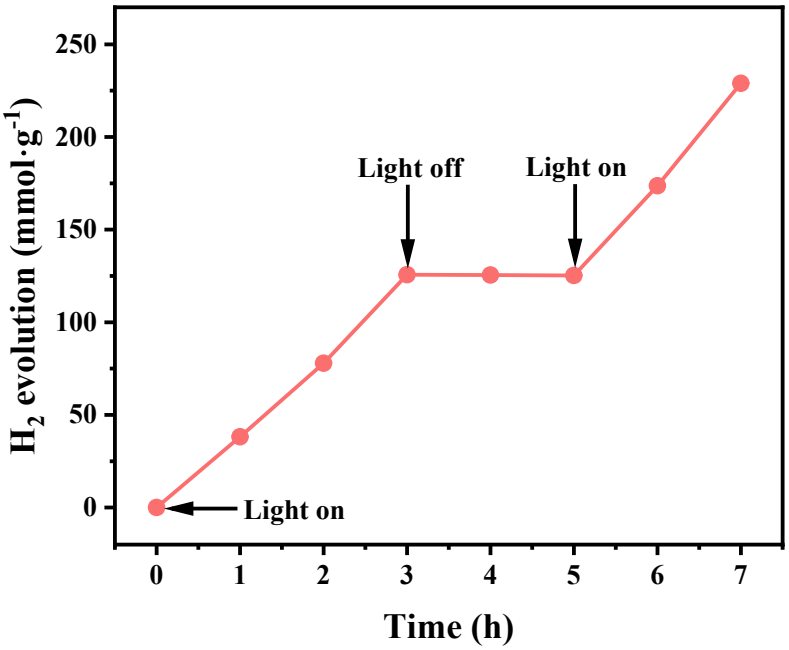

Fig. S10. H_2 production over CdS-Ru under with or without light irradiation. Reaction conditions: 2 mg catalyst, 10 mL 2 wt.% hydrazine hydrate, under LED (60 mW cm^{-2}, $\lambda = \lambda > 400$ nm) light.

Note: The cessation and subsequent resumption of H_2 generation during turning off and on the light, respectively, indicate that the production of H_2 is triggered by light irradiation.

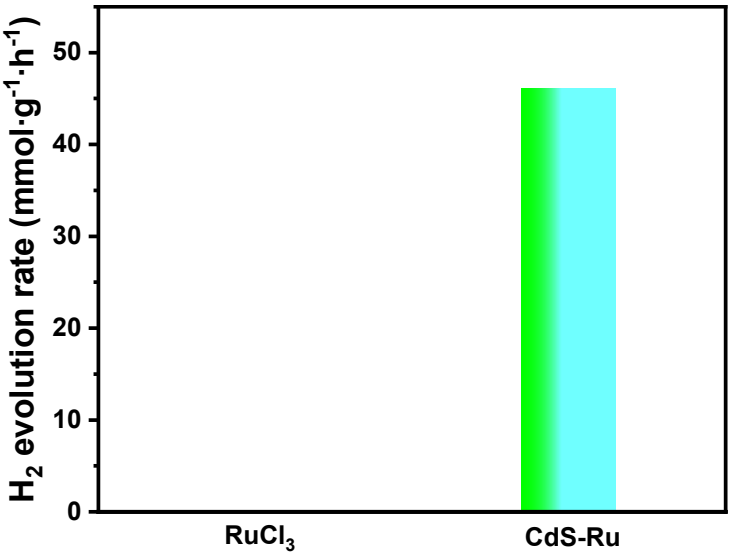

Fig. S11. H_2 production of only $RuCl_3$ and CdS-Ru. Reaction conditions: 2 mg catalyst, 10 mL 2 wt.% hydrazine hydrate, under LED (60 mW cm^{-2}, $\lambda = \lambda > 400$ nm) light.

Note: The concentration of Ru^{3+} in the $RuCl_3$ added in the photocatalytic reaction is the same as that in CdS-Ru.

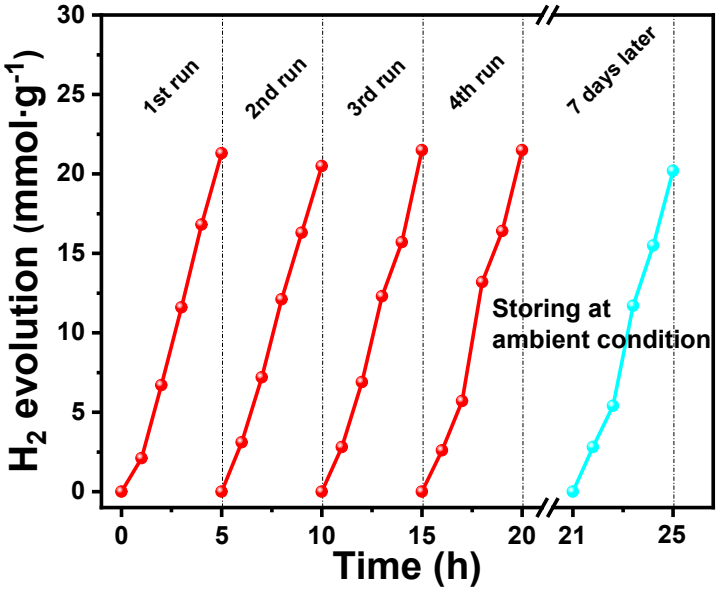

Fig. S12. The stability testing of CdS-Ru for photocatalytic H_2 evolution at ambient conditions. Reaction conditions: 2 mg catalyst, 10 mL 2 wt.% hydrazine hydrate, under LED (60 mW cm^{-2}, $\lambda > 400$ nm) light, room temperature, 1 atm, without Ar bubbling.

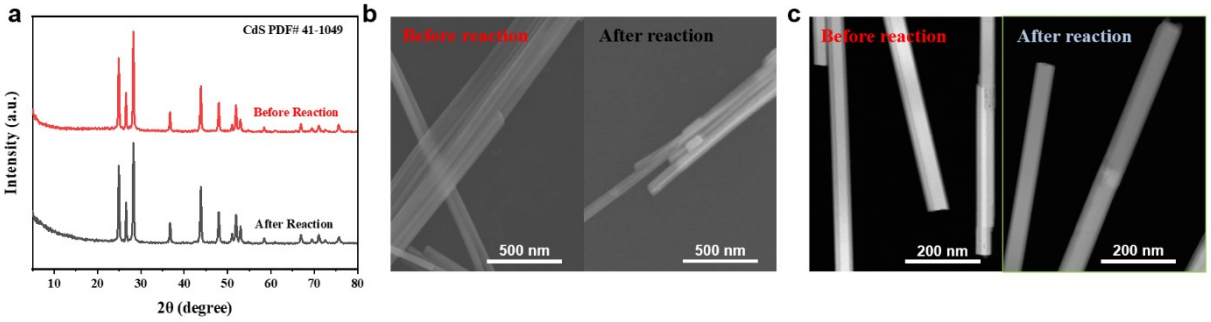

Fig. S13. (a) XRD patterns, (b) SEM images and (c) HAADF-STEM images of CdS-Ru before and after reaction.

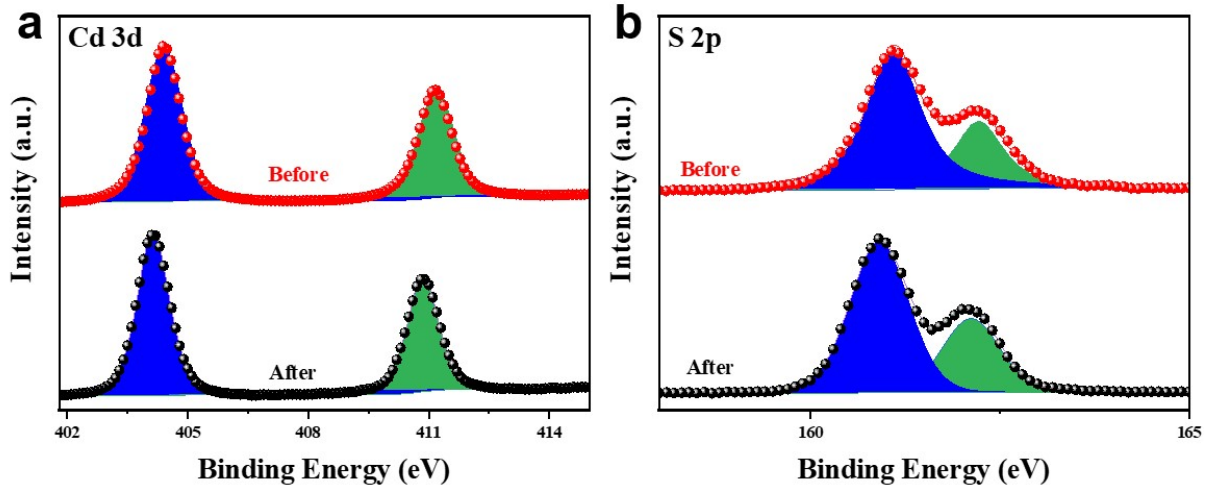

Fig. S14. High-resolution XPS spectra of (a) Cd 3d and (b) S 2p for CdS-Ru before and after reaction.

Note: In the S 2p XPS spectrum of used CdS-Ru, no redundant miscellaneous peaks related to SO_x^{2-} species were observed, indicating the absence of photocorrosion.

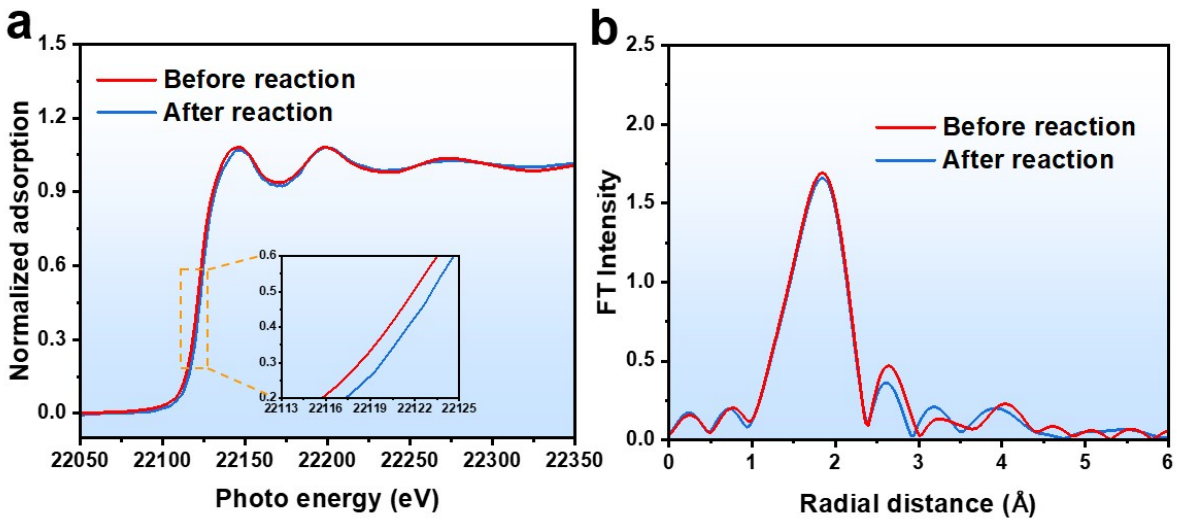

Fig. S15. (a) XANES and (b) EXAFS spectra of CdS-Ru before and after reaction.

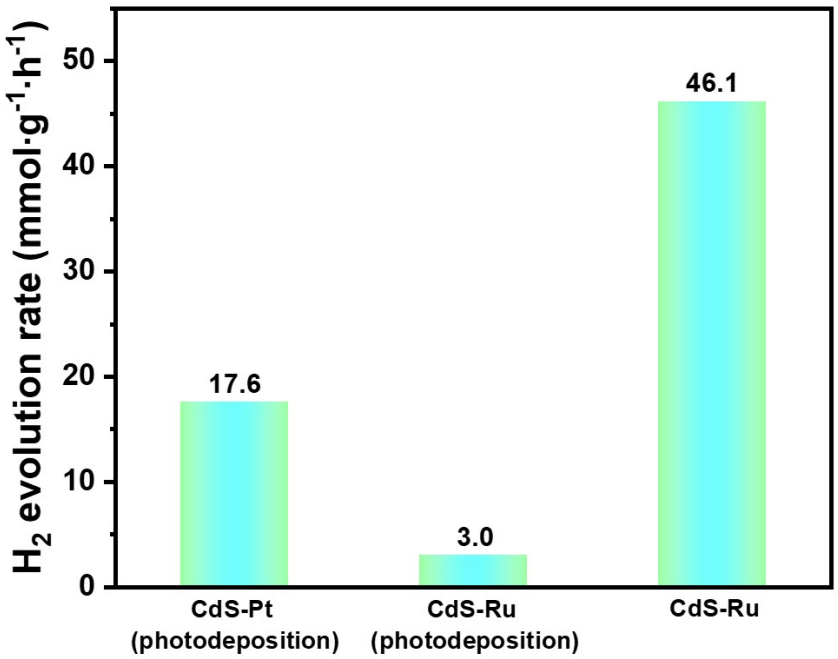

Fig. S16. H_2 production of Pt or Ru photodeposited on CdS and CdS-Ru.

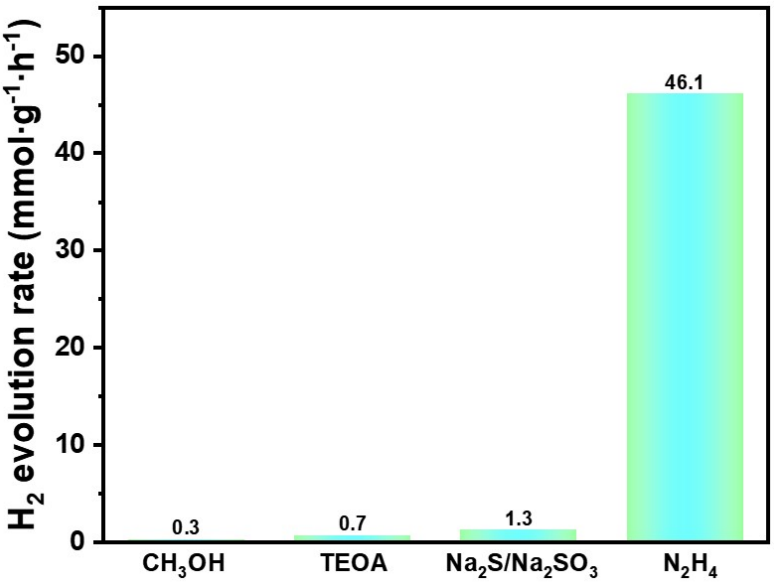

Fig. S17. H_2 production of CdS-Ru under different sacrificial agents.

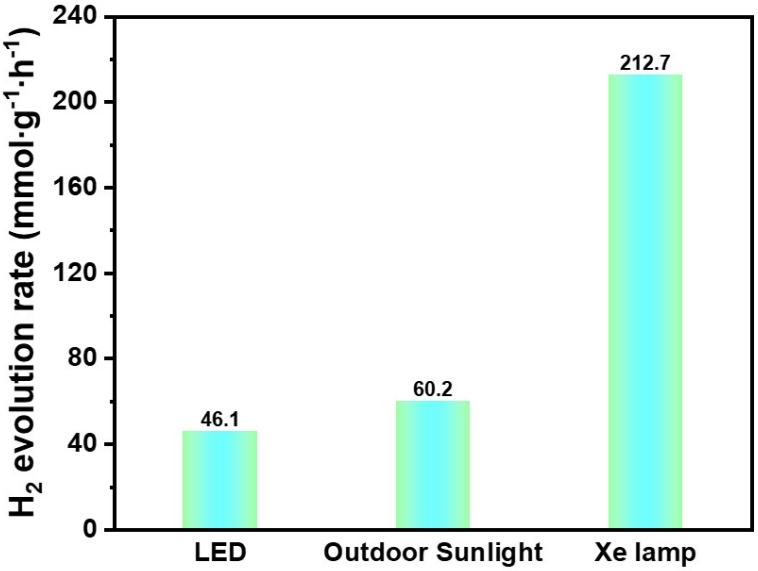

Fig. S18. H_2 production of CdS-Ru under outdoor sunlight, LED ($\lambda > 400$ nm, 60 mW cm^{-2}) lamp or 300 W Xe ($\lambda > 420$ nm, 200 mW cm^{-2}) lamp irradiation.

Reaction conditions of the outdoor environmental parameter:

Irradiation time: May 24th, from 1:30 PM to 4:30 PM;

Direct sunlight intensity: 60 mW/cm^2；

Outdoor temperature: 32 ℃；

Outdoor humidity: 45%；

Air pressure: 100.6 kPa.

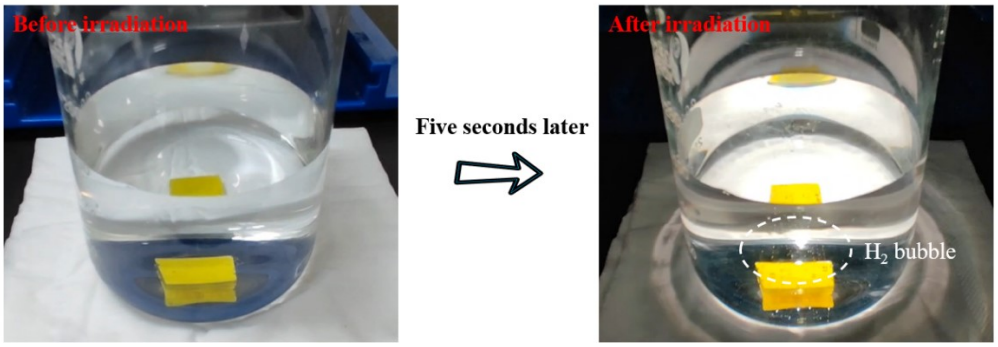

Fig. S19. Digital photo of photocatalytic H_2 production over CdS-Ru.

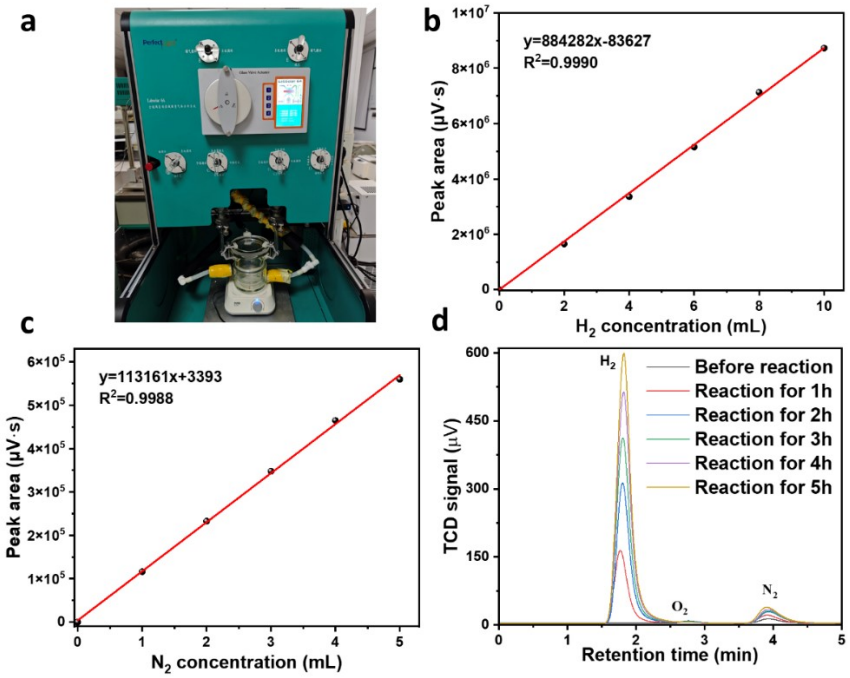

Fig. S20. (a) Photography of reaction set-up. Calibration curves for the determination of (b) H_2 and (c) N_2. (d) Time-dependent TCD signal during the reaction over CdS-Ru.

Note: To avoid the interference of O_2 and N_2 in the air, the experiment was performed on a Labsolar 6A all-glass automatic online trace gas analysis system (Beijing Perfect Light Technology Co., LTD., Fig. S19a). The calibration procedure works under the reaction conditions. Typically, 2 mg of catalyst and 10 mL of distilled H_2O containing 2 wt.% hydrazine hydrate were mixed in a 50 mL reactor. After ultrasonic treatment, connect the reactor to the online trace gas analysis system and vacuum for 10 min. A calibration line was prepared by intermittently sampling 1 mL of the standard N_2 and 2 mL of H_2 through the septum (Fig. S19b and c). The generated gas was analyzed by a GC according to the calibration line. Based on the peak area after reaction of 5 h (Fig. S19d), the N_2 and H_2 productions are respectively 4.82 mL and 10.02 mL. The ratio of produced N_2 to H_2 is determined to be 1:2.08, which is close to the theoretical value of 1:2.

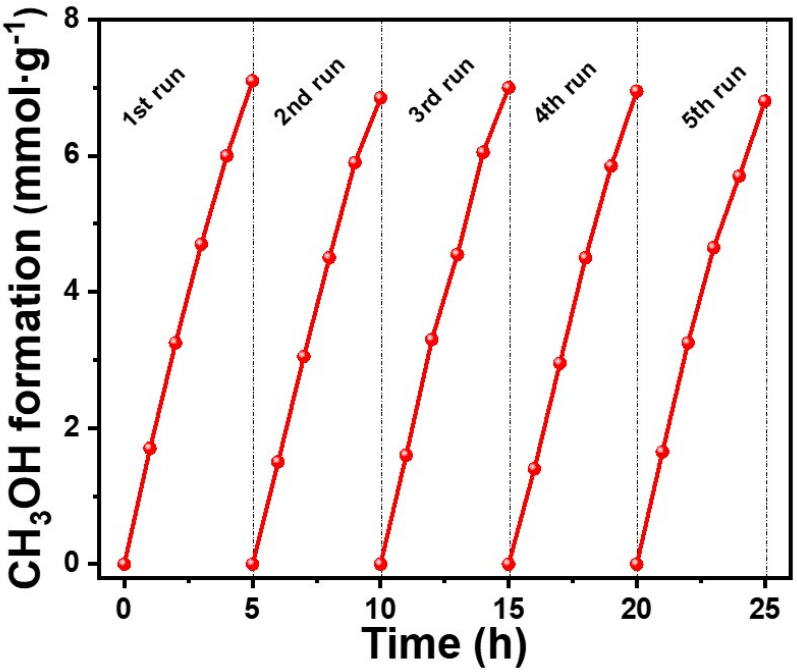

Fig. S21. The stability testing of CdS-Ru for photocatalytic CO_2 reduction to CH_3OH.

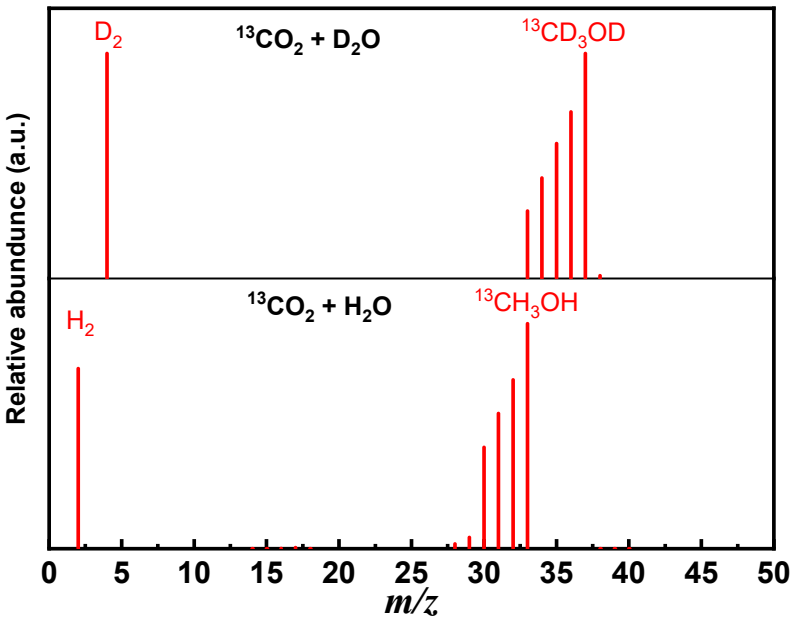

Fig. S22. Mass spectrometry results of the isotope labeling experiments with $^{13}CO_2 + H_2O$ or $^{13}CO_2 + D_2O$ as the reactant.

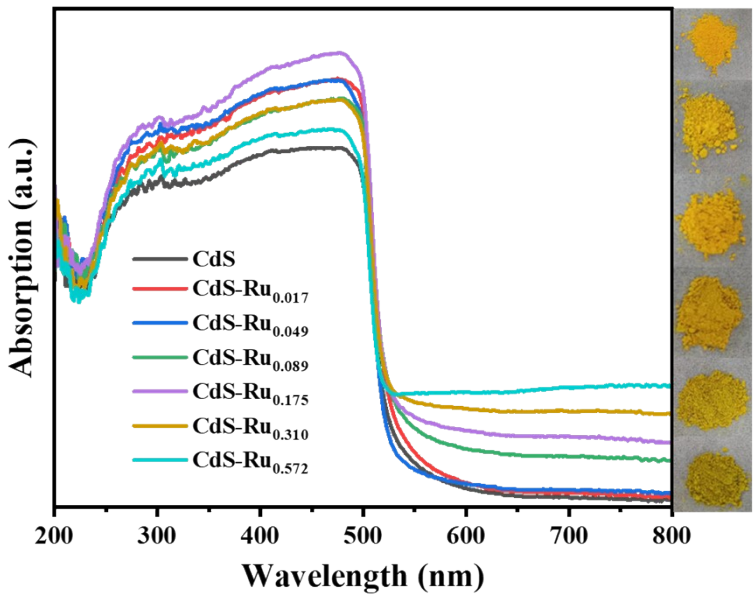

Fig. S23. UV–vis DRS spectra of CdS and CdS-Ru samples and the corresponding photographs.

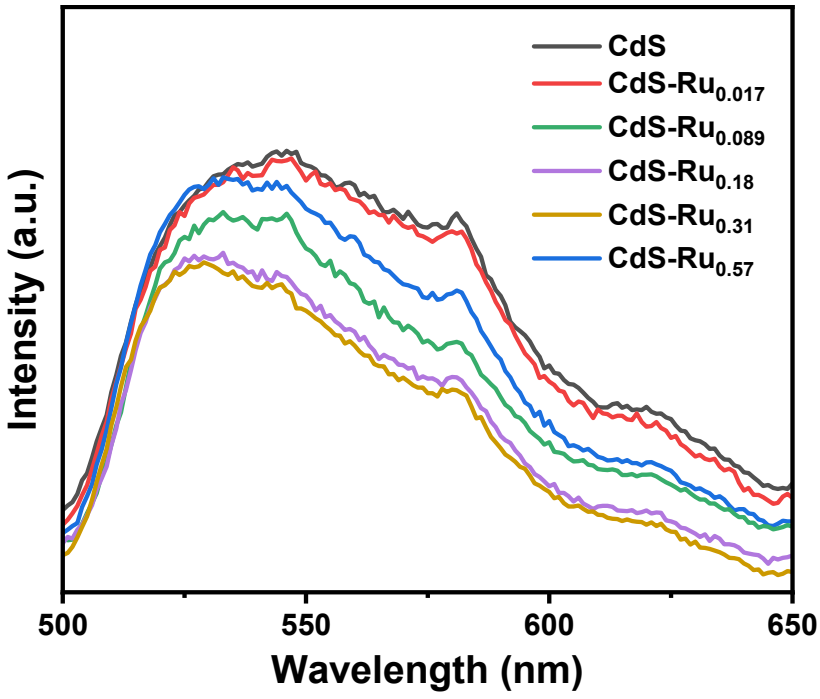

Fig. S24. PL spectra of CdS and CdS-Ru samples.

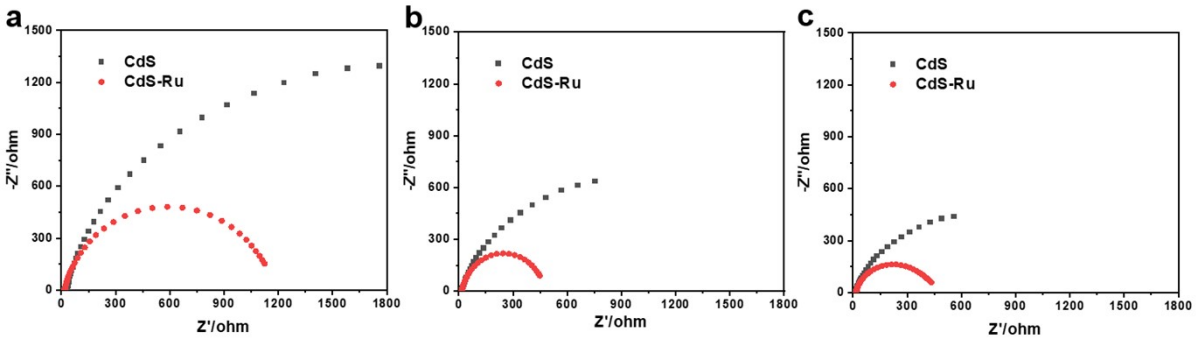

Fig. S25. EIS spectra of CdS and CdS-Ru tested at (a) 0.3 V,(b) -0.8 V and (c) -0.9 V.

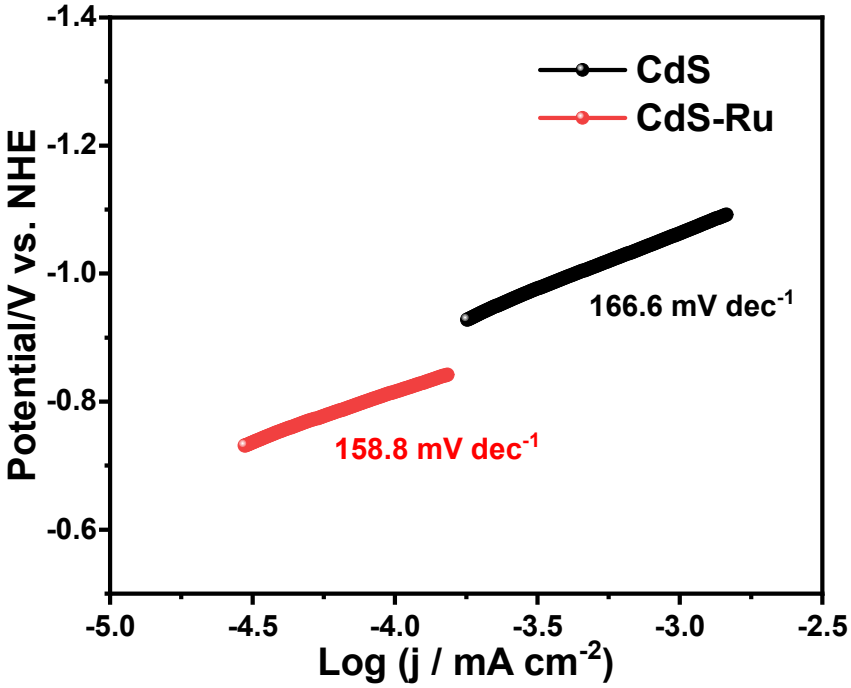

Fig. S26. Tafel slope spectra of CdS and CdS-Ru.

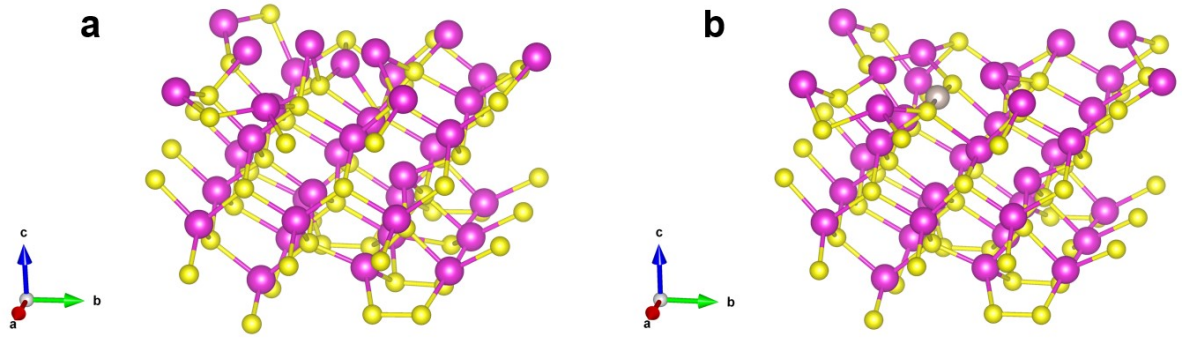

Fig. S27. The optimized structures of (a) CdS and (b) CdS-Ru during the DFT calculations.

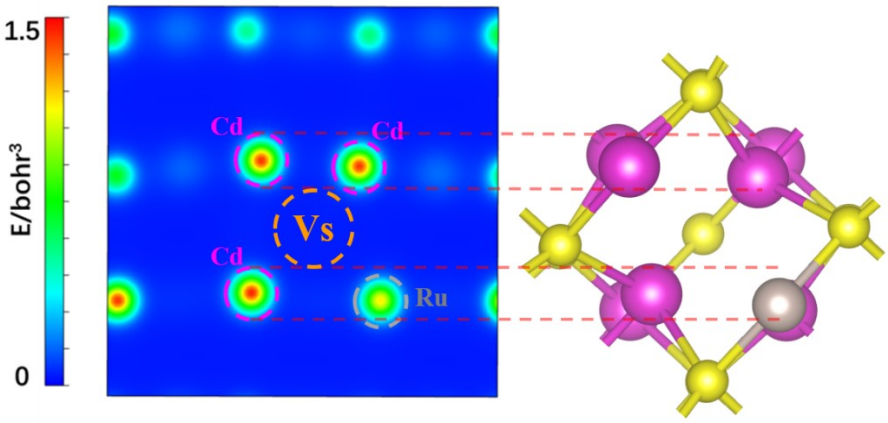

Fig. S28. The charge distribution map on the surface of CdS-Ru.

Note: It can be seen from Fig. S26 that the charge density of three Cd atoms near the V_s is increased.

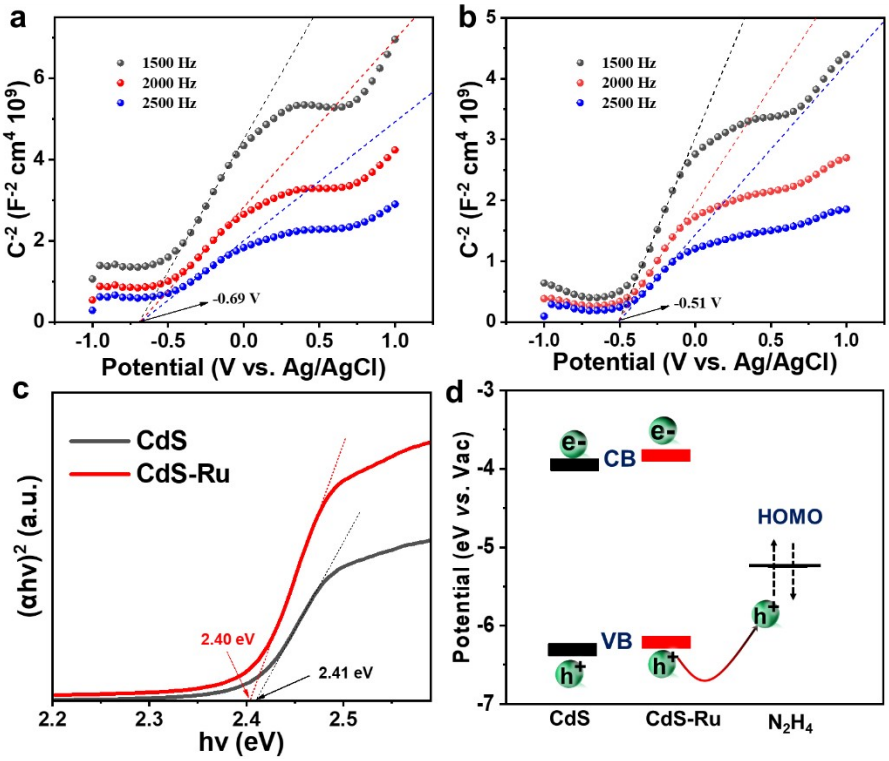

Fig. S29. Mott–Schottky plots of (a) CdS and (b) CdS-Ru. (c) Tauc plots of CdS and CdS-Ru. (d) Band diagram of CdS, CdS-Ru and hydrazine.

Note: To investigate the band structure, the conduction band (CB) of CdS and CdS-Ru was first estimated by Mott–Schottky plots (Fig. S27a and b). According to the Tauc plots (Fig. S27c), their corresponding band gaps were calculated. Finally, the combination of the above data enables to establish the complete electronic diagrams (Fig. S27d).

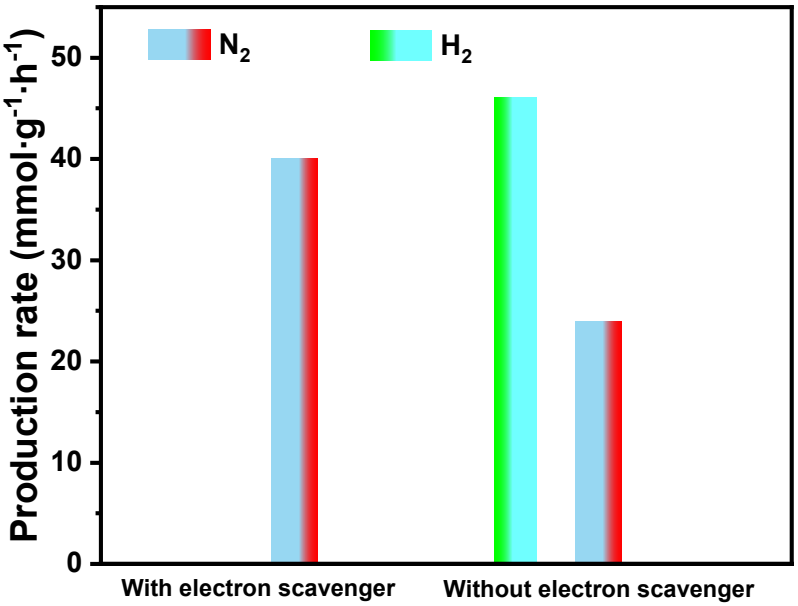

Fig. S30. H_2 production in the presence and absence of an electron scavenger.

Note: 1 mmol $KBrO_3$ was used as the electron scavenger.

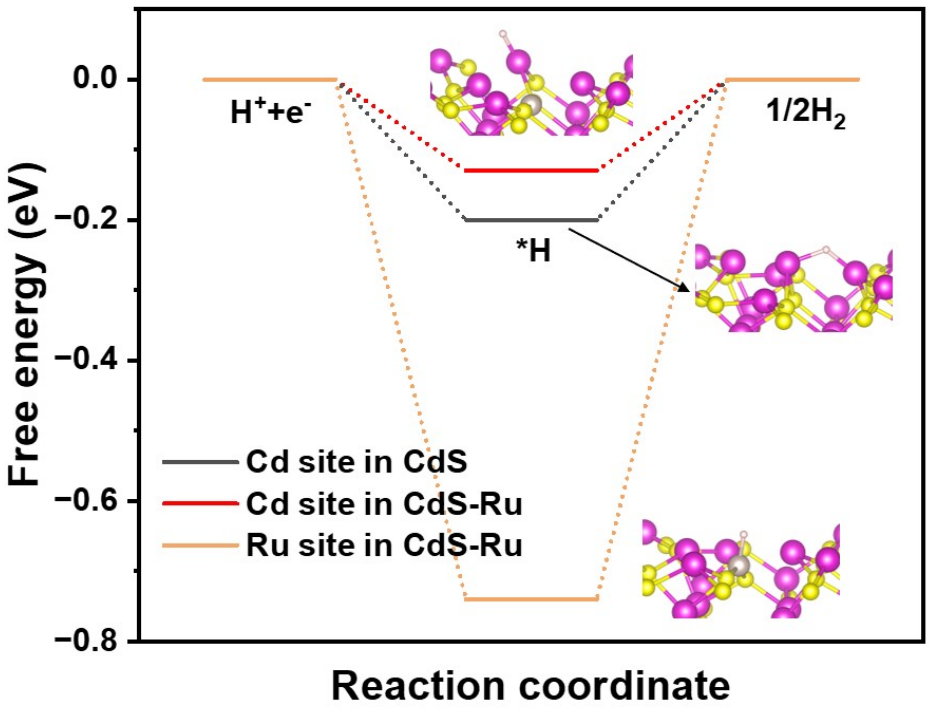

Fig. S31. Free energy profiles for the HER at different potential active sites on the CdS and CdS-Ru.

Table S1. The actual content of Ru (wt.%) in different samples.

Added content of $RuCl_3 \cdot 3H_2O$ (mg)	Actual content of Ru (wt%)	Samples
0.1	0.017	$CdS\text{-}Ru_{0.017}$
1.0	0.089	$CdS\text{-}Ru_{0.089}$
2.0	0.18	$CdS\text{-}Ru_{0.18}$
4.0	0.31	$CdS\text{-}Ru_{0.31}$
8.0	0.57	$CdS\text{-}Ru_{0.57}$

Table S2. Fitting results of EXAFS spectra at Ru K-edge. ($S_0^2 = 0.85$)

Sample	**Bond type**	**CN [a]**	**R[b] (Å)**	**σ^2 (Å^2) [c]**	**R factor [d]**
CdS-Ru	Ru-S	3.13	2.28	0.0107	0.002

NOTE: [a] CN: coordination numbers; [b] R: bond distance; [c] σ^2: Debye-Waller factors; [d] R factor: goodness of fitting.

Table S3. The actual content of Ru (wt.%) in $CdS\text{-}Ru_{0.18}$ before and after reaction.

Sample	Actual content of Ru (wt%) before reaction	Actual content of Ru (wt%) after reaction
$CdS\text{-}Ru_{0.18}$	0.18	0.18

Table S4. The detailed H_2 evolution experimental conditions of the references cited in Fig. 3d of the main text.

Catalyst marks	Light source	Reaction solution	H_2 yield	Ref.
1. CdS/MoO_X	$\lambda \geq 400$ nm, 300 W Xe lamp	10 vol% lactic acid	0.574 mmol g^{-1} h^{-1}	7
2. Sn^{2+}/CdS QDs	$\lambda \geq 420$ nm, 350 W Xe lamp	glycerol	1.61 mmol g^{-1} h^{-1}	8
3. CdS/GNR	$\lambda \geq 400$ nm, 300 W Xe lamp	10 vol% lactic acid	1.89 mmol g^{-1} h^{-1}	9
4. CdS/CoS_2	Full spectrum solar simulator	20 vol% ascorbic acid	5.54 mmol g^{-1} h^{-1}	10
5. BP-Au-CdS	$\lambda \geq 420$ nm, 300 mW cm^{-2}	0.35 M Na_2S + 0.25 M Na_2SO_3	8.6 mmol g^{-1} h^{-1}	11
6. TiO_2/MoS/CdS	$\lambda \geq 400$ nm, 300 W Xe lamp, 86 mW cm^{-2}	10 vol% lactic acid	8.95 mmol g^{-1} h^{-1}	12
7. CdS frame-in-cage particles	$\lambda \geq 400$ nm, 300 W Xe lamp	0.35 M Na_2S + 0.25 M Na_2SO_3	13.6 mmol g^{-1} h^{-1}	13
8. CdS-$Cu_{2-X}S/MoS_2$	$\lambda \geq 400$ nm, 300 W Xe lamp, 100 mW cm^{-2}	0.75 M Na_2S +1.05 M Na_2SO_3	14.18 mmol g^{-1} h^{-1}	14
9. NiS/$Zn_{0.5}Cd_{0.5}S$	$\lambda \geq 420$ nm, 300 W Xe lamp	0.35 M Na_2S + 0.25 M Na_2SO_3	16.78 mmol g^{-1} h^{-1}	15
10. Ni/ZCS QDS	$\lambda \geq 420$ nm, 300 W Xe lamp, 80 mW cm^{-2}	20 vol% TEOA	18.87 mmol g^{-1} h^{-1}	16
11. $Eu_{52}Ni_{56-x}Cd_x$/CdS	$\lambda \geq 420$ nm, 300 W Xe lamp, 200 mW cm^{-2}	0.35 M Na_2S + 0.25 M Na_2SO_3	25.35 mmol g^{-1} h^{-1}	17
12. $Cd_{0.5}Zn_{0.5}S$@halloysite	$\lambda \geq 420$ nm, 300 W Xe lamp	0.1 M Na_2S + 0.1 M Na_2SO_3	25.67 mmol g^{-1} h^{-1}	18
13. CdS(111)	$\lambda \geq 420$ nm, 350 W Xe lamp, 40 mW cm^{-2}	0.35 M Na_2S + 0.25 M Na_2SO_3	32.95 mmol g^{-1} h^{-1}	19
14. CdS/CoS_X	$\lambda \geq 420$ nm, 300 W Xe lamp	0.35 M Na_2S + 0.25 M Na_2SO_3	39.2 mmol g^{-1} h^{-1}	20
15. Sv-CdS	$\lambda \geq 420$ nm, 300 W Xe lamp, 40 mW cm^{-2}	0.35 M Na_2S + 0.25 M Na_2SO_3	41.73 mmol g^{-1} h^{-1}	21
16. CdS-Ru	$\lambda \geq 400$ nm, 5 W LED spotlights, 60 mW cm^{-2}	2 vol% N_2H_4	46.1 mmol g^{-1} h^{-1}	This work
17. Pd@CdS/PdS	$\lambda \geq 400$ nm, 300 W Xe lamp	0.1 M of Na_2S 0.1 M of Na_2SO_3	144.8 mmol g^{-1} h^{-1}	22
18. Pt_{SA}-CdS_{IS}	150 W Xenon lamp, 175 mW cm^{-2}	0.25 M Na_2S + 0.35 M Na_2SO_3	154.7 mmol g^{-1} h^{-1}	23
19. CdS-Ru	$\lambda \geq 420$ nm, 300 W Xe lamp, 200 mW cm^{-2}	2 vol% N_2H_4	212.7 mmol g^{-1} h^{-1}	This work

Table S5. The detailed CH_3OH production experimental conditions of the references cited in Fig. 3d of the main text.

Photocatalysts	Light source	Reaction solution	CH_3OH yield	Ref.
22. V-$Bi_{19}Br_3S_{27}$	λ > 720 nm, 300 W Xe lamp	$H_2O + CO_2$	0.4 μmol g^{-1} h^{-1}	24
23. $Zn_xCd_{1-x}S$/Au@g-C_3N_4	λ > 420 nm, 300 W Xe lamp	$H_2O + CO_2$	1.31 μmol g^{-1} h^{-1}	25
24. Cu_2O-RGO	500 W Xe lamp	0.1 M NaOH + $H_2O + CO_2$	4.15 μmol g^{-1} h^{-1}	26
25. α-Fe_2O_3/g-C_3N_4	λ > 420 nm, 300 W Xe lamp	$H_2O + CO_2$	5.63 μmol g^{-1} h^{-1}	27
26. NH_2-MIL-101(Fe)/CdS/g-C_3N_4	250 W high-pressure Hg lamp	$H_2O + CO_2$	6.75 μmol g^{-1} h^{-1}	28
27. $Zn_{0.2}Cd_{0.8}S$/g-C_3N_4	λ > 420 nm, 300 W Xe lamp, 100 mW cm^{-2}	$H_2O + CO_2$	11.5 μmol g^{-1} h^{-1}	29
28. mCD/CN	300 W Xe lamp, 100 mW cm^{-2}	$H_2O + CO_2$	13.9 μmol g^{-1} h^{-1}	30
29. UiO-66-NH_2	λ > 420 nm, 300 W Xe lamp	0.1 M $NaHCO_3$ + $H_2O + CO_2$	34.83 μmol g^{-1} h^{-1}	31
30. Cu-In_2O_3/TiO_2	λ < 365 nm, 500 W Xe lamp, 25 mW cm^{-2}	$H_2O + H_2 + CO_2$	35 μmol g^{-1} h^{-1}	32
31. rGO-CuO	20 W white LED	DMF + $H_2O + CO_2$	53.42 μmol g^{-1} h^{-1}	33
32. GO-3	300 W halogen lamp	$H_2O + CO_2$	172 μmol g^{-1} h^{-1}	34
33. Co/g-C_3N_4-0.2	300 W Xe lamp, 700 mW cm^{-2}	$H_2O + CO_2$	235.5 μmol g^{-1} h^{-1}	35
34. RuSA–mC_3N_4	Blue LED Light, 22 mW cm^{-2}	DMF + $H_2O + CO_2$	250 μmol g^{-1} h^{-1}	36
35. g-C_3N_4/CuO @MIL-125(Ti)	300 W Xe lamp, 32.6 mW cm^{-2}	$H_2O + CO_2$	332.4 μmol g^{-1} h^{-1}	37
36. N-In_2O_3	300 W Xe lamp	10 vol% TEOA + $H_2O + CO_2$	394 μmol g^{-1} h^{-1}	38
37. NH_2-MIL-125(Ti)	20 W white LED lamp	10 vol% TEOA + CH_3CN + H_2O + CO_2	1.97 mmol g^{-1} h^{-1}	39
38. Au@ZIF-67	150 mW cm^{-2}, Solar simulator	10 vol% TEOA + $NaHCO_3$ + H_2O + CO_2	2.5 mmol g^{-1} h^{-1}	40
39. CdS-Ru	λ > 420 nm, 300 W Xe lamp, 200 mW cm^{-2}	2 wt.% N_2H_4 + $H_2O + CO_2$	1.4 mmol g^{-1} h^{-1}	This work

Table S6. Transient current decay analysis for different samples.

Samples	A_1 (%)	τ_1 (ns)	A_2 (%)	τ_2 (ns)	τ_A (ns)
CdS	57.8	0.18	41.1	2.89	1.51
CdS-Ru	34.0	0.14	64.6	2.78	2.71

Note: The data fitting of TR-PL uses the following equations:

$$I(t) = A_1 \exp(-t/\tau_1) + A_2 \exp(-t/\tau_2) \quad (1)$$

$$\tau_A = \frac{A_1\tau_1^2 + A_2\tau_2^2}{A_1\tau_1 + A_2\tau_2} \quad (2)$$

Table S7. Spin concentration per unit volume in EPR measurements.

Samples	Spin concentration per unit volume (spins/mm^3)
CdS	2.4×10^{12}
CdS-Ru	7.3×10^{12}

Equations S1-S6.

$$*CO_2 + H^+ + e^- \rightarrow *COOH \quad (S1)$$

$$*COOH + H^+ + e^- \rightarrow *CO + H_2O \quad (S2)$$

$$*CO + H^+ + e^- \rightarrow *CHO \quad (S3)$$

$$*CHO + H^+ + e^- \rightarrow *CH_2O \quad (S4)$$

$$*CH_2O + H^+ + e^- \rightarrow *CH_3O \quad (S5)$$

$$*CH_3O + H^+ + e^- \rightarrow CH_3OH \quad (S6)$$

References

1. T. H. Chiang, H. Lyu, T. Hisatomi, Y. Goto, T. Takata, M. Katayama, T. Minegishi and K. Domen, *ACS Catal.*, 2018, **8**, 2782-2788.
2. G. Kresse and J. Furthmüller, *Comput. Mater. Sci*, 1996, **6**, 15-50.
3. G. Kresse and J. Furthmüller, *Phys. Rev. B*, 1996, **54**, 11169-11186.
4. J. P. Perdew, K. Burke and M. Ernzerhof, *Phys. Rev. Lett.*, 1996, **77**, 3865.
5. J. P. Perdew, M. Ernzerhof and K. Burke, *J. Chem. Phys.*, 1996, **105**, 9982-9985.
6. S. Grimme, *J. Comput. Chem.*, 2006, **27**, 1787-1799.
7. H. Zhang, P. Zhang, M. Qiu, J. Dong, Y. Zhang and X. W. Lou, *Adv. Mater.*, 2019, **31**, 1804883.
8. X. Xiang, B. Zhu, B. Cheng, J. Yu and H. Lv, *Small*, 2020, **16**, 2001024.
9. Y. Xia, B. Cheng, J. Fan, J. Yu and G. Liu, *Small*, 2019, **15**, 1902459.
10. P. Wang, Y. Mao, L. Li, Z. Shen, X. Luo, K. Wu, P. An, H. Wang, L. Su and Y. Li, *Angew. Chem. Int. Ed.*, 2019, **58**, 11329-11334.
11. X. Cai, L. Mao, S. Yang, K. Han and J. Zhang, *ACS Energy Lett.*, 2018, **3**, 932-939.
12. B. Sun, W. Zhou, H. Li, L. Ren, P. Qiao, W. Li and H. Fu, *Adv. Mater.*, 2018, **30**, 1804282.
13. P. Zhang, D. Luan and X. W. Lou, *Adv. Mater.*, 2020, **32**, 2004561.
14. G. Liu, C. Kolodziej, R. Jin, S. Qi, Y. Lou, J. Chen, D. Jiang, Y. Zhao and C. Burda, *ACS nano*, 2020, **14**, 5468-5479.
15. X. Zhao, J. Feng, J. Liu, W. Shi, G. Yang, G. C. Wang and P. Cheng, *Angew. Chem. Int. Ed.*, 2018, **130**, 9938-9942.
16. D. Su, J. Ran, Z. Zhuang, C. Chen, S. Qiao, Y. Li and G. Wang, *Sci. Adv.*, 2020, **6**, eaaz8447.
17. R. Chen, Z. H. Yan, X. J. Kong, L. S. Long and L. S. Zheng, *Angew. Chem. Int. Ed.*, 2018, **57**, 16796-16800.
18. S. Lin, Y. Zhang, Y. You, C. Zeng, X. Xiao, T. Ma and H. Huang, *Adv. Funct. Mater.*, 2019, **29**, 1903825.
19. Y. Zhao, C. Shao, Z. Lin, S. Jiang and S. Song, *Small*, 2020, **16**, 2000944.
20. X. Zhang, H. Liang, H. Li, Y. Xia, X. Zhu, L. Peng, W. Zhang, L. Liu, T. Zhao and C. Wang, *Angew. Chem. Int. Ed.*, 2020, **132**, 3313-3319.
21. J. He, L. Hu, C. Shao, S. Jiang, C. Sun and S. Song, *ACS nano*, 2021, **15**, 18006-18013.
22. Q. Sun, N. Wang, J. Yu and J. C. Yu, *Adv. Mater.*, 2018, **30**, 1804368.
23. P. Sharma, M. Sharma, M. Dearg, M. Wilding, T. J. Slater and C. R. A. Catlow, *Angew. Chem. Int. Ed.*, 2023, **135**, e202301239.

24. J. Li, W. Pan, Q. Liu, Z. Chen, Z. Chen, X. Feng and H. Chen, *J. Am. Chem. Soc.*, 2021, **143**, 6551-6559.
25. P. Madhusudan, R. Shi, S. Xiang, M. Jin, B. N. Chandrashekar, J. Wang, W. Wang, O. Peng, A. Amini and C. Cheng, *Appl. Catal. B-Environ.*, 2021, **282**, 119600.
26. A. Wang, X. Li, Y. Zhao, W. Wu, J. Chen and H. Meng, *Powder Technol.*, 2014, **261**, 42-48.
27. H. Guo, M. Chen, Q. Zhong, Y. Wang, W. Ma and J. Ding, *J. CO_2 Util.*, 2019, **33**, 233-241.
28. R. Manna, G. Bhattacharya, P. Sardar, S. Raj, A. Jain and A. N. Samanta, *Chem. Eng. Sci.*, 2024, **288**, 119811.
29. H. Guo, J. Ding, S. Wan, Y. Wang and Q. Zhong, *Appl. Surf. Sci.*, 2020, **528**, 146943.
30. Y. Wang, X. Liu, X. Han, R. Godin, J. Chen, W. Zhou, C. Jiang, J. F. Thompson, K. B. Mustafa and S. A. Shevlin, *Nat. Commun.*, 2020, **11**, 2531.
31. J. Meng, Q. Chen, J. Lu and H. Liu, *ACS Appl. Mater. Interfaces*, 2018, **11**, 550-562.
32. M. Tahir, B. Tahir, N. A. S. Amin and H. Alias, *Appl. Surf. Sci.*, 2016, **389**, 46-55.
33. R. Gusain, P. Kumar, O. P. Sharma, S. L. Jain and O. P. Khatri, *Appl. Catal. B-Environ.*, 2016, **181**, 352-362.
34. H.-C. Hsu, I. Shown, H.-Y. Wei, Y.-C. Chang, H.-Y. Du, Y.-G. Lin, C.-A. Tseng, C.-H. Wang, L.-C. Chen and Y.-C. Lin, *Nanoscale*, 2013, **5**, 262-268.
35. M. Ma, Z. Huang, D. E. Doronkin, W. Fa, Z. Rao, Y. Zou, R. Wang, Y. Zhong, Y. Cao and R. Zhang, *Appl. Catal. B-Environ.*, 2022, **300**, 120695.
36. P. Sharma, S. Kumar, O. Tomanec, M. Petr, J. Zhu Chen, J. T. Miller, R. S. Varma, M. B. Gawande and R. Zbořil, *Small*, 2021, **17**, 2006478.
37. N. Li, X. Liu, J. Zhou, W. Chen and M. Liu, *Chem. Eng. J.*, 2020, **399**, 125782.
38. Y. Yang, Y.-X. Pan, X. Tu and C.-j. Liu, *Nano Energy*, 2022, **101**, 107613.
39. J. O. Olowoyo, U. Saini, M. Kumar, H. Valdes, H. Singh, M. O. Omorogie, J. O. Babalola, A. V. Vorontsov, U. Kumar and P. G. Smirniotis, *J. CO_2 Util.*, 2020, **42**, 101300.
40. J. Becerra, D.-T. Nguyen, V.-N. Gopalakrishnan and T.-O. Do, *ACS Appl. Energy Mater.*, 2020, **3**, 7659-7665.